Article

MOFs-Derived Porous NiFe$_2$O$_4$ Nano-Octahedrons with Hollow Interiors for an Excellent Toluene Gas Sensor

Yanlin Zhang [1], Chaowei Jia [1], Qiuyue Wang [1], Quan Kong [1], Gang Chen [1,2], Hongtao Guan [1,2,*] and Chengjun Dong [1,2,*]

[1]   School of Materials Science and Engineering, Yunnan University, Kunming 650091, China
[2]   Yunnan Province Key Lab of Micro-Nano Materials and Technology, Yunnan University, Kunming 650091, China
[*]   Correspondence: htguan06@ynu.edu.cn (H.G.); dongchjun@hotmail.com or dongcj@ynu.edu.cn (C.D.)

check for updates

Abstract: Toluene is extensively used in many industrial products, which needs to be effectively detected by sensitive gas sensors even at low-ppm-level concentrations. Here, NiFe$_2$O$_4$ nano-octahedrons were calcinated from NiFe-bimetallic metal-organic framework (MOFs) octahedrons synthesized by a facile refluxing method. The co-existence of p-Phthalic acid (PTA) and 3,3-diaminobenzidine (DAB) promotes the formation of smooth NiFe-bimetallic MOFs octahedrons. After subsequent thermal treatment, a big weight loss (about 85%) transformed NiFe$_2$O$_4$ nanoparticles (30 nm) into NiFe$_2$O$_4$ porous nano-octahedrons with hollow interiors. The NiFe$_2$O$_4$ nano-octahedron based sensor exhibited excellent gas sensing properties for toluene with a nice stability, fast response, and recovery time (25 s/40 s to 100 ppm toluene), and a lower detection limitation (1 ppm) at 260 °C. The excellent toluene-sensing properties can not only be derived from the hollow interiors combined with porous nano-octahedrons to favor the diffusion of gas molecules, but also from the efficient catalytic activity of NiFe$_2$O$_4$ nanoparticles.

Keywords: MOFs; NiFe$_2$O$_4$; octahedron; gas sensor; toluene

1. Introduction

Toluene is one kind of a colorless substance with a unique aromatic odor that is widely used in commercial products and industrial applications. Unfortunately, toluene is seriously harmful to human health as it strongly affects the nervous system to induce brain function disturbances and damage to the kidneys or liver [1,2]. In addition, toluene is considered as one of the important biomarkers for a diagnosis of lung cancer [3,4]. Moreover, toluene is easily flammable when the temperature is above 4.4 °C [5,6]. Due to the harmful effects of toluene, it is of great urgency to be able to effectively detect toluene. To date, various gas sensors have been developed. In particular, resistive-based gas sensors on a metal oxide base are the most attractive with respect to their cost-effective, versatile, and simple fabrication techniques. Recently, p-type oxide semiconductors have been used as sensing materials due to their good catalysts and multivalent characteristics that favor the selective oxidation of various volatile organic compounds (VOCs) [7]. Although many p-type oxide semiconductors such as NiO [8], CuO [9], Co$_3$O$_4$ [10], Cr$_2$O$_3$ [11], Mn$_3$O$_4$ [12], and so on have been reported to have potential for gas sensors, it is still far less than their counterpart, n-type oxide semiconductors.

Recently, spinel ferrites, MFe$_2$O$_4$ (M = Zn, Ni, Co, Cu, Mn, Cd, etc.), which are materials that include two types of transition metals, have stood out due to their robust catalytic activity as exhibiting significant potential applications in various fields. In particular, a few of them such as ZnFe$_2$O$_4$ [13,14],

NiFe$_2$O$_4$ [15–22], CoFe$_2$O$_4$ [23], MnFe$_2$O$_4$ [24], Ni$_{1-X}$Co$_X$Fe$_2$O$_4$ [25], and NiCuZn ferrites [26] have been reported to be greatly promising in the electrical properties of gas sensors and humidity sensors. More interesting, NiFe$_2$O$_4$ with various microstructures have been prepared so far to effectively detect acetone [14–17], ammonia [18], NO$_2$ [19], n-propanol [20], and triethylamine [21]. However, intense efforts are expected to further enhance the sensing properties of the NiFe$_2$O$_4$ based gas sensor. Designing NiFe$_2$O$_4$ with unique microstructures is considered to be the most highly promising way. To date, templates (hard template, soft template, and bio-template) are widely used to tune the morphologies of products [27–29]. In particular, soft templates are beneficial for the synthesis of different materials to tune the morphologies under relatively mild experimental conditions. Typically, self-assembly occurs involving the soft template, precursor, and solvent molecules. Organic ligands can be used as a sufficient soft template to coordinate metal ions to obtain a unique structure. For instance, Prussian blue analogue derived porous NiFe$_2$O$_4$ nanocubes have been synthesized, which exhibit sensitivity and selectivity to acetone at low operating temperatures [16].

Today, MOFs have attracted particular attention as sacrificial templates to obtain designable nanoarchitectures [30] with intriguing properties aside from their direct applications in energy storage [31], catalysis [32], electronic devices [33], drug delivery [34], adsorbents [35], separation [36], etc. Among uncountable MOFs, Fe-containing MOFs have been extensively studied thus far due to their good diversity, low toxicity, excellent stability, and easy functionality [37]. Taking the template of MIL-88-Fe, spindle like α-Fe$_2$O$_3$ with porous structures have been reported to enhance electrochemical performance [38]. In addition, the NiFe bimetallic MOFs have been synthesized by metal Ni incorporation, which is further converted to ternary oxides of NiFe$_2$O$_4$. Song et al. obtained hollow NiFe$_2$O$_4$ microspindles from NiFe bimetallic MOFs, illustrating a high sensitivity for acetone detection [14]. Zhang et al. prepared 1D α-Fe$_2$O$_3$/NiFe$_2$O$_4$ heterojunction, which showed an improved response to acetone vapors using NiFe-bimetallic MOFs [39]. Previously, we prepared 1D porous NiFe$_2$O$_4$ nanorods using 2-aminoterephthalic acid as the ligand, which showed excellent selectivity and sensitivity to toluene [40]. Nevertheless, as of now, tuning the NiFe$_2$O$_4$ microstructures on a NiFe-bimetallic MOFs template base is still developing and in the early stage.

As discussed above, we herein combined both PTA and DAB to prepare NiFe-bimetallic MOFs octahedrons. After thermal treatment, porous NiFe$_2$O$_4$ nano-octahedrons with hollow interiors were obtained by assembling a large number of nanoparticles. The gas sensor based on NiFe$_2$O$_4$ nano-octahedrons showed excellent gas sensing properties for toluene detection at low-ppm-levels with good reproducibility, a fast response and recovery time, and a lower detection limit at the optimum operating temperature. Thus, the gas sensing mechanism for the NiFe$_2$O$_4$ based sensor is understood in detail.

2. Materials and Methods

2.1. Materials Synthesis

All the starting reagents were of analytical grade (AR grade) and unpurified. Highly pure water (18 MΩ cm at 25 °C) was used throughout the experiments. First, the octahedron NiFe-bimetallic MOFs were synthesized through a refluxing method, as schematically shown in Figure 1, which were further transferred into NiFe$_2$O$_4$ with thermal treatment. Typically, 9 mmol of p-Phthalic acid (PTA) was completely dissolved in 50 mL *N,N*-Dimethylformamide (DMF). At the same time, 0.3 mmol 3,3-diaminobenzidine (DAB) was dissolved into 30 mL ethanol. Next, the ethanol was slowly added to form a homogenous solution. When the desirable NiCl$_2$·6H$_2$O (0.5 mmol) and FeCl$_2$·4H$_2$O (1 mmol) were dissolved into 10 mL DMF, it was dropped into the above mixture with vigorous stirring for 30 min. The whole mixture was refluxed at 120 °C by an oil bath under magnetic stirring for 3 h. Subsequently, the NiFe-bimetallic MOFs were collected after washing several times with ethanol and deionized water, and then air dried at 60 °C for 24 h. Finally, the as-prepared NiFe-precursor was

thermally treated at 350 °C for 1 h, and then at 500 °C for a further hour in air at a heating rate of 3 °C/min. Therefore, the NiFe$_2$O$_4$ nano-octahedrons were obtained.
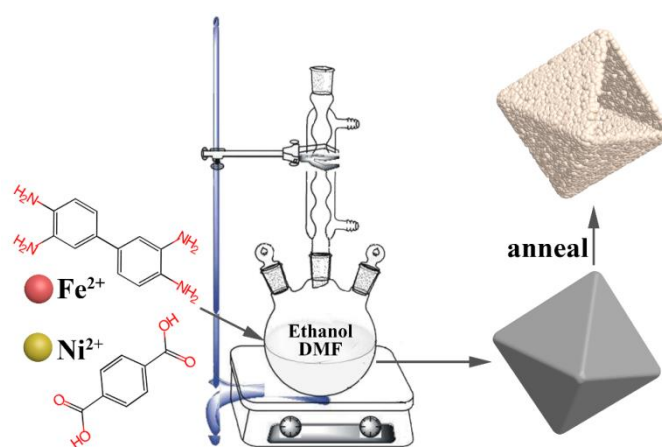
Figure 1. Schematic illustration of the fabrication of the NiFe$_2$O$_4$ nano-octahedrons.

2.2. Materials Characterization

The structure of NiFe$_2$O$_4$ was characterized using a Rigaku TTRIII x-ray diffraction with Cu K$_\alpha$ radiation (1.540 Å). A FEI QUANTA 200 microscope was used to investigate the morphology of NiFe$_2$O$_4$ and the NiFe-precursor. The TEM and HRTEM images and corresponding elemental mapping images were obtained by a JEOL JEM-2100 microscope. X-ray photoelectron spectroscopy (XPS) spectra were also measured under Al K_α X-ray radiation at 15 kV, which were calibrated by a C 1s peak (284.6 eV). An American TA SDT-2960 thermal analyzer was used to examine the transformation from the NiFe-precursor to the final NiFe$_2$O$_4$ (heating rate of 10 °C/min). After degassing at 300 °C for 3 h under vacuum, a Micromeritics ASAP 2010 automated sorption analyzer was applied to carry out the nitrogen adsorption/desorption measurements.

2.3. Fabrication and Measurement of the Gas Sensor

Following previous works, the gas sensor was fabricated and tested [41,42]. The slurry was formed by dispersing the NiFe$_2$O$_4$ powder in proper deionized water, which was coated on the surface of an alumina tube. In order to form a resistive-based gas sensor, a pair of Au electrodes were passed at each end of the tube, which was further connected by Pt wires. In general, the thickness of the sensing film was about 0.6–0.8 mm. After drying at 120 °C for 2 h, the sensor was annealed at 400 °C for 2 h in air. Then, a Bakelite base was connected to the Pt wires and a Ni–Cr alloy wire was inserted into the tube to perform measurements in a WS-30A system. During the test, the dry air was taken as the reference to mix with an evaporated target solution to obtain the desired concentration. As a typical p-type material, the response (β) of the sensor is generally defined as R_g/R_a, (R_a and R_g represent the resistance of the sensor in air and in the presence of target gases, respectively). Furthermore, the response and recovery time were evaluated by the time for 90% of the initial equilibrium resistance change in the adsorption and desorption processes.

3. Results

NiFe-bimetallic MOFs octahedrons were synthesized by a simple refluxing method, as schematically shown in Figure 1, which was used as the self-sacrificial template for NiFe$_2$O$_4$ fabrication. It is clear that uniform NiFe-MOFs octahedrons were well-defined with an average size of about 300 nm, as shown in the inset of Figure 2a. Close observation revealed that these NiFe-MOFs octahedrons were smooth on the surface. The as-prepared NiFe-MOFs octahedrons were further thermally transformed into NiFe$_2$O$_4$ nano-octahedrons in an air atmosphere at a heating rate of

3 °C/min. After thermal treatment, it can be seen that the configuration of the NiFe-MOFs octahedrons was perfectly preserved, as shown in Figure 2a,b. However, the $NiFe_2O_4$ nano-octahedrons were assembled by a large number of nanoparticles, leading to a rough surface. Importantly, the hollow interiors were strongly confirmed by a broken $NiFe_2O_4$ nano-octahedron in the inset of Figure 2b.
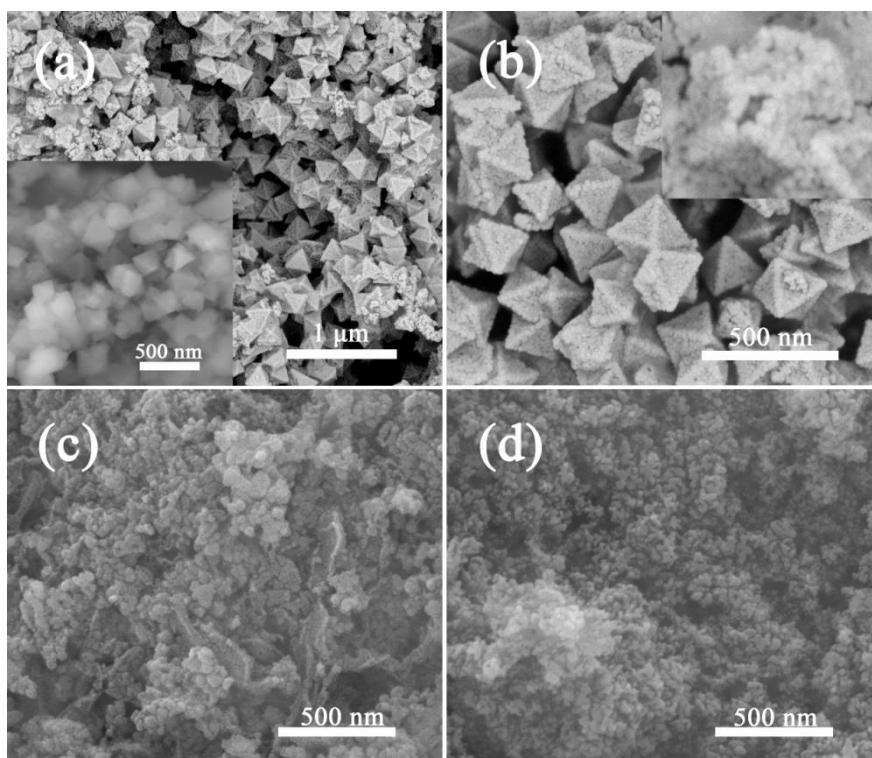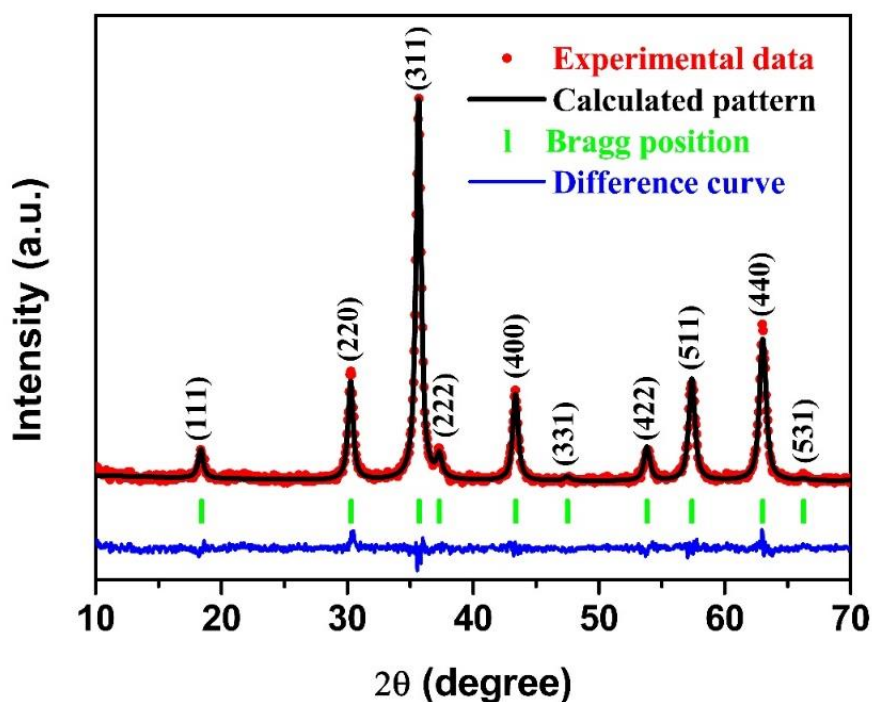

Figure 2. FESEM images of $NiFe_2O_4$ nano-octahedrons in low (**a**) and high magnification (**b**), and $NiFe_2O_4$ synthesized without DAB (**c**), or PTA (**d**). Insets show the FESEM images of NiFe-bimetallic MOFs (**a**) and the hollow interior of $NiFe_2O_4$ (**b**).

The crystal structure of the $NiFe_2O_4$ nano-octahedrons was studied by XRD measurements, as shown in Figure 3. Compared with the JCPDS: 54-0964, as indicated by the Bragg position at the bottom of the figure, a pure specimen was identified with a cubic $NiFe_2O_4$ structure (space-group: $Fd\bar{3}m$). The appearance of no other diffraction peaks confirmed the high phase purity. The structural parameters were further analyzed by Rietveld refinement based on the Maud program [43]. The difference curve was not greatly fluctuated, which is a sign that the calculated pattern had good consistence with the experimental data in the whole recorded angles from 10–70°. The lattice parameters of a = 8.341092 Å were obtained. Moreover, the crystallite size of around 25.56 nm was estimated. These strong and narrow diffraction XRD peaks are persuasive evidence that an individual $NiFe_2O_4$ phase was completely crystallized by the above thermal treatment of NiFe-bimetallic MOFs.

In order to gain further insight into the structural details on $NiFe_2O_4$ nano-octahedrons, TEM and HRTEM measurements were carried out. The TEM observations in Figure 4a demonstrate that a large number of ultrafine nanoparticles (an average diameter of about 30 nm) were homogeneously distributed within the interconnected walls of the hollow octahedrons. From a featured octahedron in Figure 4b, the hollow interior was clearly distinguished by the dark boundary, indicating that the hollow interior was formed by porous walls of around 50 nm in thickness. The lattice fringes of 0.48 nm in the HRTEM image (Figure 4c) could be assigned to the (111) interplane spacing of $NiFe_2O_4$. Moreover, the porous structure and the specific surface area of $NiFe_2O_4$ was investigated using the nitrogen adsorption–desorption isotherms, as shown in Figure 5. Clearly, the sample showed an obvious H3 hysteresis loop, which can be described as a type IV isotherm, implying the presence

of a mesoporous and hollow structure. The pore size distribution of the $NiFe_2O_4$ nano-octahedrons calculated using the BJH method was centered at 31.78 nm, as shown in the inset of Figure 5. A BET surface area of 43.89 m^2/g was obtained. This should offer our $NiFe_2O_4$ a sufficient interface and porous structure to facilitate the gas sensing properties. Furthermore, EDS elemental mapping images of individual $NiFe_2O_4$ nano-octahedrons (Figure 4d–g) demonstrate the homogeneous coexistence of Ni, Fe, and O elements.

Figure 3. XRD patterns for the experimental and Rietveld refinement data for the $NiFe_2O_4$ nano-octahedrons.
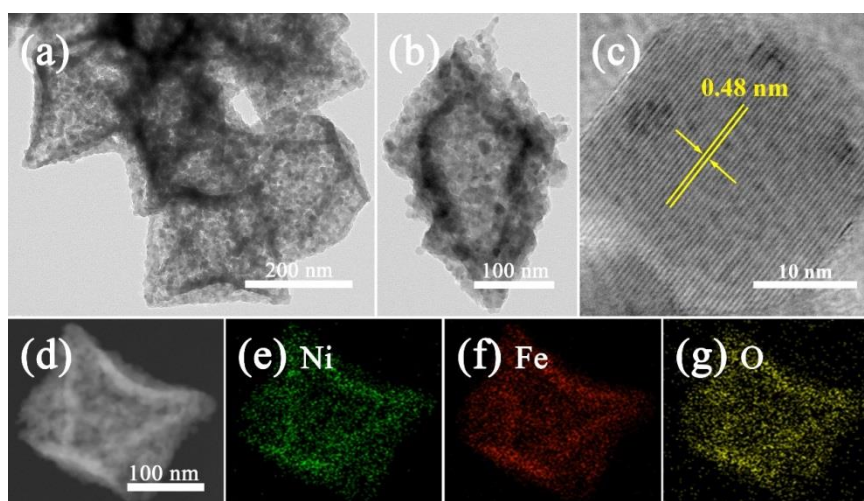

Figure 4. TEM (**a**,**b**) and HRTEM (**c**) images of the $NiFe_2O_4$ nano-octahedrons and elemental mapping images of Ni (**e**), Fe (**f**), and O (**g**) for an individual $NiFe_2O_4$ nano-octahedron (**d**).
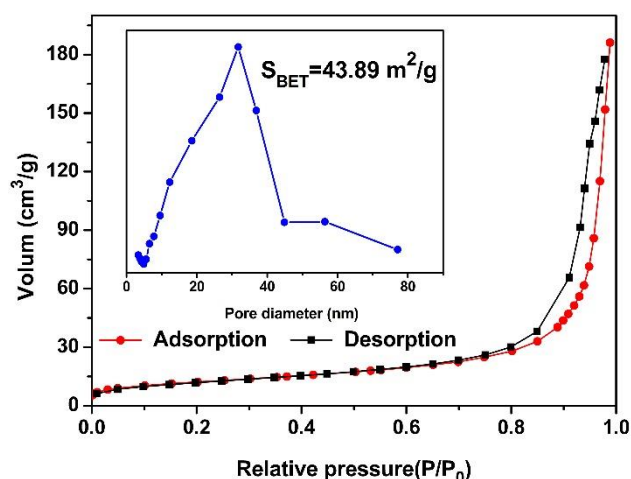
Figure 5. Nitrogen adsorption–desorption isotherm along with the pore size distribution of the $NiFe_2O_4$ nano-octahedrons.

Thermogravimetric measurements were performed to explore the transformation from NiFe-bimetallic MOFs to $NiFe_2O_4$. From the TG curve shown in Figure 6, it can be seen that about 6.55% weight loss was observed in the temperature blow 120 °C, which originated from the loss of absorbed water in the precursor. By further increasing the temperature to 350 °C, around 45.60% weight loss occurred due to the decomposition of organic ligands in the NiFe-bimetallic MOFs. Up to 425 °C, 15% weight was maintained. Accordingly, a clear exothermal peak at 412.66 °C in the DSC curve was observed, suggesting the transformation of NiFe-bimetallic MOFs to $NiFe_2O_4$. It is noteworthy that the large weight loss can be reasonably explained by the large numbers of organic ligands in the NiFe-bimetallic MOFs synthesized by coupling DAB with PTA in a mixed solution of DMF and ethanol.
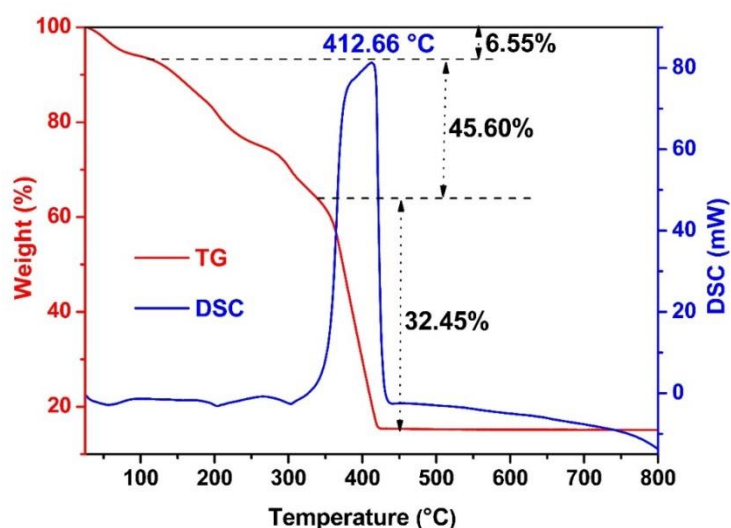
Figure 6. TGA–DSC curves of transformation from NiFe-bimetallic MOFs to $NiFe_2O_4$.

Taken together, the porous $NiFe_2O_4$ nano-octahedrons were thermally obtained from NiFe-bimetallic MOFs synthesized by a facile refluxing route, which was assembled by a large number of nanoparticles. The existence of abundant organic ligands was revealed by the large weight loss in TG measurements due to the cooperative effects of PTA and DAB in the mixture of DMF and ethanol. It has been reported that Schiff-base polymer spheres have been obtained using certain amounts of PTA and DAB in ethanol at 80 °C under stirring-reflux, which can be further transformed

into N-doped porous carbons [44]. To understand the growth mechanism, contrast experiments were conducted only dependent on PTA or DAB following the same experimental process, respectively. Without DAB, the $NiFe_2O_4$ nanoparticles were observed with some sheets, as shown in Figure 2c. In the presence of DAB, the $NiFe_2O_4$ nanoparticles seemed to be more uniform (Figure 2d). Therefore, the combination of PTA and DAB plays a critical role in coordinating with the metal ions to produce octahedral NiFe-bimetallic MOFs through the refluxing approach.

To evaluate the potential practicality and reliability of the gas sensor based on $NiFe_2O_4$ nano-octahedrons, the fundamental properties of a gas sensor were thoroughly studied. The responses of our $NiFe_2O_4$ based sensor to 100 ppm toluene at various operating temperatures from 220–300 °C are shown in Figure 7a. Clearly, the responses kept increasing to reach a maximum at 260 °C and then started to decrease with further increased temperatures. At lower temperatures, the slow diffusion of the tested gas molecules and the insufficient thermal energy to accelerate the reaction between the gas molecules and adsorbed oxygen species is believed to result in a relatively low response. The existence of oxygen species will be given in the XPS analysis below. Although enough thermal energy is available at higher temperatures, it could reduce the gas adsorption capacity from the sensing materials, leading to a decreased response [45,46]. Hence, the gas sensing measurements in the following were performed at 260 °C.
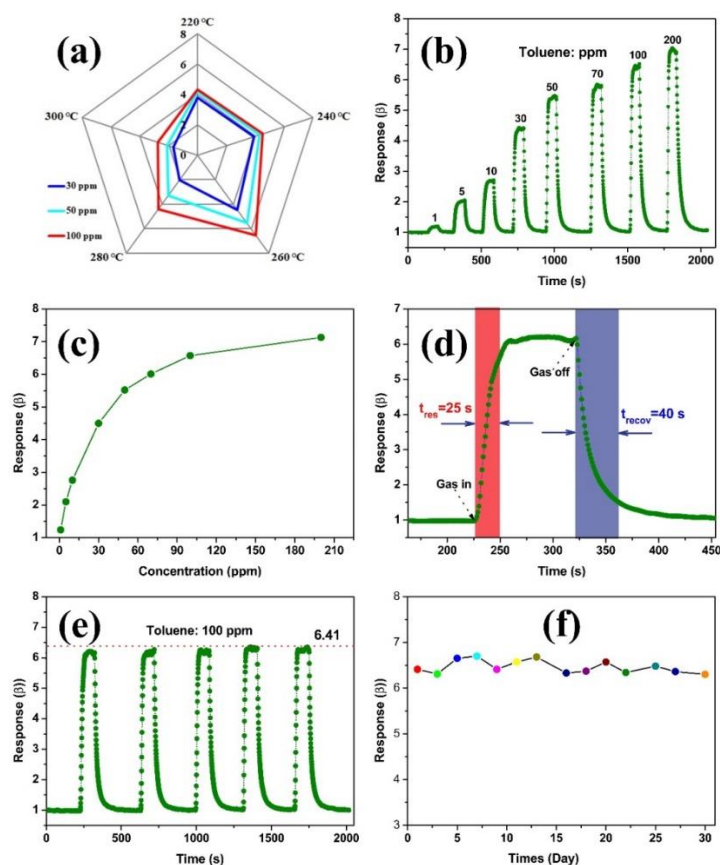
Figure 7. Polar graphs shows the gas responses of gas sensors based on $NiFe_2O_4$ nano-octahedrons as 30, 50, and 100 ppm toluene vs. operating temperatures from 220–300 °C (**a**). Dynamic sensing plot of sensors based on $NiFe_2O_4$ nano-octahedrons upon exposure to toluene (**b**). Concentration dependent response curve vs. the toluene concentrations (1–200 ppm) (**c**). Response/recovery graph to 100 ppm toluene (**d**), and reproducibility of sensor upon exposure (five cycles) to 100 ppm toluene at 260 °C (**e**). Long-term stability (30 days) of sensor to 100 ppm toluene (**f**).

Figure 7b shows the dynamic responses of the $NiFe_2O_4$ nano-octahedrons to 1–200 ppm toluene. It can be seen that a stepwise distribution of the curves appeared by switching dry air and a certain

concentration of the target gas. With increasing toluene concentrations, the responses of the sensor rapidly increased. Specifically, the sensor showed approximately responses of 1.24, 2.10, 2.76, 4.50, 5.52, 6.01, 6.57, and 7.13 to 1, 5, 10, 30, 50, 70, 100, and 200 ppm of toluene, respectively, as shown in Figure 7b. It is noteworthy that the responses sharply increased at lower toluene concentrations because the coverage of the gas molecules was low on the surface of the sensing material (Figure 7c). In our case, the sensor was capable of detecting 1 ppm toluene. With the further increase in the toluene concentration, the material surface was gradually covered completely. Thus, the rising trend of responses gradually slowed down, indicating the saturation of the sensor to some extent [47]. Taking 100 ppm toluene as an example, the sensor exhibited fast response/recovery times of 25 s/40 s (Figure 7d). In addition, the responses were almost maintained for the five cyclic toluene exposures, as displayed in Figure 7e, which showed good repeatability within a fluctuation of 2.2%. Furthermore, the long-term stability of the gas sensor was evaluated. The continuous tests were carried out over 30 days with a one day interval while exposing the sensor to 100 ppm toluene. As shown in Figure 7f, the sensor exhibited small deviations (6.2%) during the test over 30 days, demonstrating the good stability of the $NiFe_2O_4$. Importantly, our $NiFe_2O_4$ based gas sensor showed a comparable sensing performance with typical p-type nanomaterials, as summarized in Table 1.

Table 1. Comparison of toluene sensing performance among the gas sensors based on typical p-type materials.

Materials	Microstructures	Concentration (ppm)	T (°C)	Response	Limit of Detection	Ref.
NiO	Flower-like	5	250	2.63	0.5 ppm	[48]
NiO	Nanoparticle	200	210	1.6	100 ppm	[49]
CuO	Flower	500	260	2.5	10 ppm	[50]
Co_3O_4	Nanorod	200	200	35	10 ppm	[51]
Co_3O_4	Nanosheet	100	150	6.08	1 ppm	[52]
Co_3O_4	Microsphere	100	180	2.2		[53]
Cr_2O_3	Microsphere	100	170	33.64	1 ppm	[54]
$Ag-LaFeO_3$	Nanoparticle	5	215	24	5 ppm	[55]
$NiGa_2O_4-NiO$	Nanosphere	100	230	12.7	0.5 ppm	[56]
$NiFe_2O_4$	Ordered mesoporous	1	230	77.3	2 ppb	[57]
$NiFe_2O_4$	Hexagonal biyramid	200	140	5.73	5 ppm	[20]
$NiFe_2O_4$	Nano-octahedron	100	260	6.41	1 ppm	This work

The selectivity generally demonstrated the capability that the gas sensor had to distinguish the target gas without any interference, which is also important for practical applications. Figure 8 compares the sensing response of the $NiFe_2O_4$ nano-octahedron based sensor to 100 ppm toluene, acetone, ethanol, methanol, isopropanol, n-butyl alcohol, formaldehyde, ammonia, and toluene at the same operating temperature of 260 °C. Against the interferences, the gas sensor showed a relatively selective and sensitive detection toward toluene. One plausible explanation for the selective detection of toluene could be ascribed to the excellent catalytic nature of p-type $NiFe_2O_4$ to toluene, leading to more released electrons back to the $NiFe_2O_4$ materials after the reactions of target molecules on the surface [58,59]. Moreover, the optimum operating temperature of 260 °C could provide suitable active energy to promote the reactions of toluene on the $NiFe_2O_4$ surface. Thus, a big change of resistance for the sensor occurred, which exhibits excellent sensing performances.
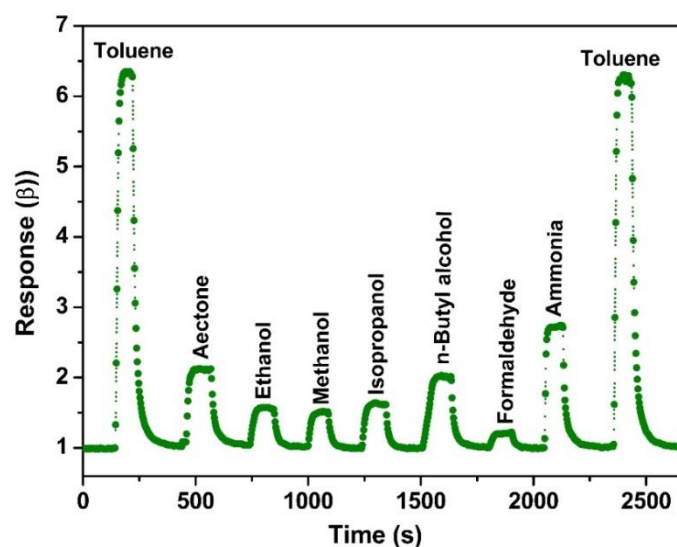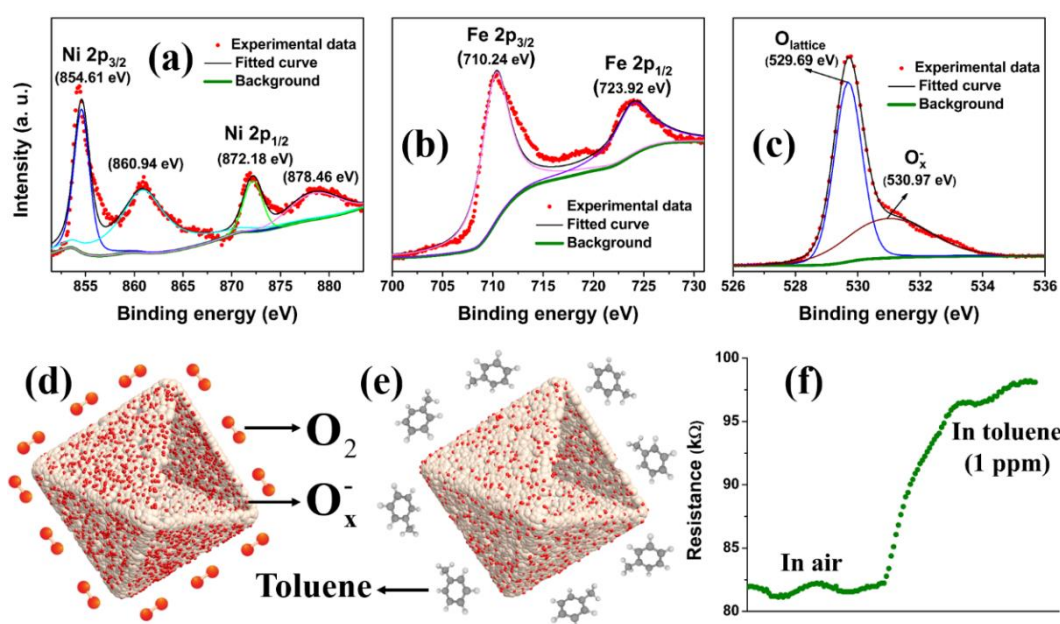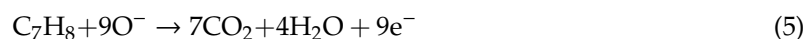
Figure 8. Selectivity of NiFe$_2$O$_4$ nano-octahedrons to 100 ppm of various gases at 260 °C.

As defined above, the sensing response of a semiconductor is dependent on the variation of resistance, which is highly related to both the surface compositions and valance states of the elements in the sensing materials. Therefore, the XPS investigation was conducted, as shown in Figure 9. The high resolution XPS analysis of the Ni 2p spectra in Figure 9a displays the specific peaks of Ni 2p$_{1/2}$ and Ni 2P$_{3/2}$ at the binding energies of 8723.18 eV and 854.61 eV with two apparent satellite peaks at 878.46 eV and 860.94 eV, respectively. Meanwhile, the Fe-related fitting peaks with binding energy values of 723.92 eV and 710.24 eV, corresponded well with Fe 2p$_{1/2}$ and Fe 2p$_{3/2}$, respectively (Figure 9b). The XPS results verify the Ni(II) and Fe(III) in the NiFe$_2$O$_4$ [39]. In particular, the O 1s XPS spectrum, as shown in Figure 9c, could be resolved by two peaks located at 529.69 eV and 530.97 eV, implying various oxygen contributions. Specifically, the peak at the low binding energy of 529.69 eV is typically assigned to that of lattice oxygen (O$_{lattice}$), which is unreactive with target gases. In contrast, the well-resolved peak at a higher binding energy of 530.97 eV was assigned to surface adsorbed oxygen species, which evolved into O$_2^-$, O$^-$, and O^{2-}. These oxygen species are believed to play a critical role in reacting with the target gas to determine the gas sensing properties [60]. As is well known, O$_2$ has a stronger electron affinity, making it adsorbed on the surface of NiFe$_2$O$_4$ even at room temperature though a physical process.

When the operating temperature rose to 260 °C, a more stable adsorbed oxygen species can be formed. Thus, the mechanism governing the sensing properties of NiFe$_2$O$_4$ nano-octahedrons can be systematically discussed by the following process. As a typical p-type semiconductor, holes are the charge carriers in NiFe$_2$O$_4$. The evolution of absorbed oxygen into oxygen species, as confirmed by the above XPS analysis, will reduce the electrons in the sensing materials (Figure 9d). Therefore, the rich existence of holes generates a hole accumulation layer on the very surface of NiFe$_2$O$_4$, leading to a highly conductive state in the air. After exposure to a reductive gas atmosphere such as toluene, the reaction between these oxygen species and target gas molecules can release the trapped electrons back (Figure 9e), which results in the conductivity of the NiFe$_2$O$_4$ based sensor decreasing greatly. Thus, a high resistance state can obviously appear. For instance, a real resistance of about 82 kΩ was measured in the air for the NiFe$_2$O$_4$ based sensor, as shown in Figure 9f. After exposure to even 1 ppm toluene, the resistance dramatically increased to approximately 98 kΩ. When the NiFe$_2$O$_4$ based sensor was switched to air again, sufficient oxygen molecules alternatively adsorbed on the NiFe$_2$O$_4$ surface. As a result, the resistance restored its initial status, leading to the achievement of a whole response–recovery period. In contrast with the electrical conductivity seen in previous reports [61,62], our nano-octahedron NiFe$_2$O$_4$ exhibited good electrical conductivity with low resistivity. The variation

ratio of resistance is heavily determined by the sensing materials and the concentrations of the target gas. The possible reactions are clarified in the following [1,63]

$$O_2(\text{gas}) \rightarrow O_2(\text{adsorbed}) \tag{1}$$

$$O_2(\text{adsorbed}) + e^- \rightarrow O_2^- \tag{2}$$

$$O_2^- + e^- \rightarrow 2O^- \tag{3}$$

$$O^- + e^- \rightarrow O^{2-} \tag{4}$$

$$C_7H_8 + 9O^- \rightarrow 7CO_2 + 4H_2O + 9e^- \tag{5}$$

$$C_7H_8 + 9O^{2-} \rightarrow 7CO_2 + 4H_2O + 18e^- \tag{6}$$

Figure 9. High-resolution XPS spectra for Ni 2p (**a**), Fe 2p (**b**), and O 1s (**c**), and a schematic illustration of the sensing mechanism of the NiFe$_2$O$_4$ nano-octahedrons in air (**d**), and in toluene (**e**) with the obverse real resistance change in air and 1 ppm toluene (**f**).

In short, the unique assembly of NiFe$_2$O$_4$ nanoparticles into porous nano-octahedrons with hollow interiors can provide enough specific surface areas and space and rich active sites to catalyze toluene. The native features of NiFe$_2$O$_4$ may be suitable for the toluene catalyst at an optimum operating temperature due to the reversible redox reaction of Ni$^{2+} \leftrightarrow$ Ni^{3+}, Fe$^{2+} \leftrightarrow$ Fe^{3+} [39]. Specifically, the as-prepared mesopore nano-octahedrons with hollow interiors easily facilitate the fast diffusion of gas molecules in reaching and departing from the sensing surface. In addition, a large number of NiFe$_2$O$_4$ may offer more active sites to boost the reaction between the target gas molecules and oxygen species. Thus, the as-synthesized NiFe$_2$O$_4$ nano-octahedrons show excellent sensing properties to low-ppm-level toluene. The response and selectivity could be further enhanced by proper doping, or appropriately coupling with other nanomaterials or functionalizing with noble metal nanoparticles. For instance, the Ni$_{0.33}$Co$_{0.67}$Fe$_2$O$_4$ microspheres showed the highest gas-sensing sensitivity to toluene due to their rich oxygen vacancies and large specific surface area [64]. Compared with individual α-Fe$_2$O$_3$ and NiFe$_2$O$_4$, the 1D α-Fe$_2$O$_3$/NiFe$_2$O$_4$ heterojunction showed better gas-sensing properties for acetone detection due to the enhanced charge separation and carrier4 depletion layer at the interface [39].

4. Conclusions

In summary, porous $NiFe_2O_4$ nano-octahedrons were successfully synthesized using a facile refluxing route via a simple and direct pyrolysis of NiFe-bimetallic MOFs. The cooperative effects of PTA and DAB play a critical role in the formation of octahedral NiFe-bimetallic MOFs precursors. The gas sensing performance of the $NiFe_2O_4$ based sensor was studied for toluene detection. As a result, the gas sensor exhibited the advantages of long-term stability (30 days), excellent repeatability, short response (25 s) and recovery (40 s) time, and a lower detection limitation (1 ppm). These resulting sensing properties may stem from the decent specific surface area (43.89) with a porous structure, hollow interiors, small size (30 nm), and the catalytic nature of $NiFe_2O_4$. More importantly, the easy fabrication strategy can be properly extended for the preparation of other well-defined micro-/nano-structures using both PTA and DAB as coordinated ligands.

Author Contributions: Y.Z. synthesized the samples, performed the gas sensing experiments, and wrote the main manuscript. C.J., Q.K., and Q.W. performed the basic characterization. G.C. analyzed the data. H.G. and C.D. proposed the research topic and edited the paper.

Conflicts of Interest: The authors declare no conflict of interest.

References

1.   Mirzaei, A.; Kim, J.H.; Kim, H.W.; Kim, S.S. Resistive-based gas sensors for detection of benzene, toluene and xylene (BTX) gases: A review. *J. Mater. Chem. C* **2018**, *6*, 4342–4370. [CrossRef]

2.   Malik, R.; Tomer, V.K.; Vandna, C.; Dahiya, M.S.; Nehra, S.P.; Duhan, S.; Kailasam, K. A low temperature, highly sensitive and fast response toluene gas sensor based on In(III)-SnO_2 loaded cubic mesoporous graphitic carbon nitride. *Sens. Actuators B Chem.* **2018**, *255*, 3564–3575. [CrossRef]

3.   Peng, G.; Tisch, U.; Adams, O.; Hakim, M.; Shehada, N.; Broza, Y.Y.; Billan, S.; Bortnyak, R.A.; Kuten, A.; Haick, H. Diagnosing lung cancer in exhaled breath using gold nanoparticles. *Nat. Naotechnol.* **2009**, *4*, 669–673. [CrossRef] [PubMed]

4.   Kim, N.H.; Choi, S.J.; Yang, D.J.; Bae, J.; Park, J.; Kim, I. Highly sensitive and selective hydrogen sulfide and toluene sensors using Pd functionalized WO_3 nanofibers for potential diagnosis of halitosis and lung cancer. *Sens. Actuators B Chem.* **2014**, *193*, 574–581. [CrossRef]

5.   Donald, J.M.; Hooper, K.; Rich, C.H. Reproductive and developmental toxicity of toluene: A review. *Environ. Health Perspect.* **1991**, *94*, 237–244. [CrossRef] [PubMed]

6.   Yücel, M.; Takagi, M.; Walterfang, M.; Lubman, D.I. Toluene misuse andlong-term harms: A systematic review of the neuropsychological andneuroimaging literature. *Neurosci. Biobehav. Rev.* **2008**, *32*, 910. [CrossRef] [PubMed]

7.   Kim, H.J.; Lee, J.H. Highly sensitive and selective gas sensors using p-type oxide semiconductors: Overview. *Sens. Actuators B Chem.* **2014**, *192*, 607–627. [CrossRef]

8.   Majhi, S.M.; Naik, G.K.; Lee, H.J.; Song, H.G.; Lee, C.R.; Lee, I.H.; Yu, Y.T. Au@NiO core-shell nanoparticles as a p-type gas sensor: Novel synthesi, characterization, and their gas sensing properties with sensing mechanism. *Sens. Actuators B Chem.* **2018**, *268*, 223–231. [CrossRef]

9.   Hu, J.; Zou, C.; Su, Y.J.; Li, M.; Han, Y.T.; Kong, E.S.W.; Yang, Z.; Zhang, Y.F. An ultrasensitive NO_2 gas sensor based on a hierarchical Cu_2O/CuO mesocrystal nanoflower. *J. Mater. Chem. A* **2018**, *6*, 17120–17131. [CrossRef]

10. Liu, Y.; Wang, Y.; Ikram, M.; Lv, H.; Chang, J.B.; Li, Z.K.; Ma, L.F.; Rehman, A.U.; Lu, G.; Chen, J.H.; et al. Facile synthesis of highly dispersed Co_3O_4 nanoparticles on expanded, thin black phosphorus for a ppb-level NO_2 gas sensor. *ACS Sens.* **2018**, *3*, 1576–1583. [CrossRef]

11. Kim, B.Y.; Yoon, J.W.; Lim, K.; Park, S.H.; Yoon, J.W.; Lee, J.H. Hollow spheres of $CoCr_2O_4$-Cr_2O_3 mixed oxides with nanoscale heterojunctions for exclusive detection of indoor xylene. *J. Mater. Chem. C* **2018**, *6*, 10767–10774. [CrossRef]

12. Bigiani, L.; Maccato, C.; Carraro, G.; Gasparotto, A.; Sada, C.; Comini, E.; Barreca, D. Tailoring vapor-phase fabrication of Mn_3O_4 nanosystems: From synthesis to gas-sensing applications. *ACS Appl. Nano Mater.* **2018**, *1*, 2962–2970. [CrossRef]

13. Dong, C.J.; Liu, X.; Xiao, X.C.; Du, S.F.; Wang, Y.D. Monodisperse $ZnFe_2O_4$ nanospheres synthesized by a nonaqueous route for a highly selective low-ppm-level toluene gas sensor. *Sens. Actuators B Chem.* **2017**, *239*, 1231–1236. [CrossRef]

14. Virumbrales, M.; Regino, S.P.; Torralvo, M.J.; Veronica, B.G. Mesoporous Silica Matrix as a Tool for Minimizing Dipolar Interactions in $NiFe_2O_4$ and $ZnFe_2O_4$ Nanoparticles. *Nanomaterials* **2017**, *7*, 151. [CrossRef] [PubMed]

15. Song, X.Z.; Sun, F.F.; Dai, S.T.; Lin, X.; Sun, K.M.; Wang, X.F. Hollow $NiFe_2O_4$ microspindles derived from Ni/Fe bimetallic MOFs for highly sensitive acetone sensing at low operating temperatures. *Inorg. Chem. Front.* **2018**, *5*, 1107–1114. [CrossRef]

16. Wang, X.F.; Ma, W.; Jiang, F.; Cao, E.S.; Sun, K.M.; Cheng, L.; Song, X.Z. Prussian blue analogue derived porous $NiFe_2O_4$ nanocubes for low concentration acetone sensing at low working temperature. *Chem. Eng. J.* **2018**, *338*, 504–512. [CrossRef]

17. Zhou, T.T.; Zhang, T.; Zeng, Y.; Zhang, R.; Lou, Z.; Deng, J.N.; Wang, L.L. Structure-driven efficient $NiFe_2O_4$ materials for ultra-fast response electronic sensing platform. *Sens. Actuators B Chem.* **2018**, *225*, 1436–1444. [CrossRef]

18. Zhang, L.; Jiao, W.L. The effect of microstructure on the gas properties of $NiFe_2O_4$ sensors: Nanotube and nanoparticle. *Sens. Actuators B Chem.* **2015**, *216*, 293–297. [CrossRef]

19. Anggraini, S.A.; Yoshida, S.; Ikeda, H.; Miura, N. Selective NO_2 detection using YSZ-based amperometric sensor attached with $NiFe_2O_4$ (+Fe_2O_3) sensing electrode. *Sens. Actuators B Chem.* **2018**, *259*, 30–35. [CrossRef]

20. Song, X.Z.; Meng, Y.L.; Chen, X.; Sun, K.M.; Wang, X.F. Hollow $NiFe_2O_4$ hexagonal biyramids for high-performance n-propanol sensing at low temperature. *New J. Chem.* **2015**, *5*, 76229–76248. [CrossRef]

21. Chu, X.F.; Jiang, D.L.; Zheng, C.M. The preparation and gas-sensing properties of $NiFe_2O_4$ nanocubes and nanorods. *Sens. Actuators B Chem.* **2007**, *123*, 739–797. [CrossRef]

22. Yadav, R.S.; Kuřitka, I.; Vilčáková, J.; Machovský, M.; Škoda, D.; Urbánek, P.; Masař, M.; Gořalik, M.; Urbánek, M.; Kalina, L.; et al. Polypropylene Nanocomposite Filled with Spinel Ferrite $NiFe_2O_4$ Nanoparticles and In-Situ Thermally-Reduced Graphene Oxide for Electromagnetic Interference Shielding Application. *Nanomaterials* **2019**, *9*, 621. [CrossRef] [PubMed]

23. Yuan, Y.; Wang, B.; Wang, C.; Li, X.D.; Huang, J.Q.; Zhang, H.B.; Xia, F.; Xiao, J.Z. Effects of $CoFe_2O_4$ electrode microstructure on the sensing properties for mixed potential NH_3 sensor. *Sens. Actuators B Chem.* **2017**, *239*, 462–466. [CrossRef]

24. Zhang, L.; Wang, G.; Yu, F.; Zhang, Y.; Ye, B.C.; Li, Y.C. Facile synthesis of hollow $MnFe_2O_4$ nanoboxes based on galvanic replacement reaction for fast and sensitive VOCs sensor. *Sens. Actuators B Chem.* **2018**, *258*, 589–596. [CrossRef]

25. Virlan, C.; Tudorache, F.; Pui, A. Increased sensibility of mixed ferrite humidity sensors by subsequent heat treatment. *Int. J. Appl. Ceram. Technol.* **2017**, *14*, 1174–1182. [CrossRef]

26. Virlan, C.; Tudorache, F.; Pui, A. Tertiary NiCuZn ferrites for improved humidity sensors: A systematic study. *Arab. J Chem.* **2018**. [CrossRef]

27. Liu, Y.D.; Goebl, J.; Yin, Y.D. Templated synthesis of nanostructured materials. *Chem. Soc. Rev.* **2013**, *42*, 2610–2653. [CrossRef]

28. Petkovich, N.D.; Stein, A. Controlling macro- and mesostructures with hierarchical porosity through combined hard and soft templating. *Chem. Soc. Rev.* **2013**, *42*, 3721–3739. [CrossRef] [PubMed]

29. Huang, J.L.; Lin, L.Q.; Sun, D.H.; Chen, H.M.; Yang, D.P.; Li, Q.B. Bio-inspired synthesis of metal nanomaterials and applications. *Chem. Soc. Rev.* **2015**, *44*, 6330–6374. [CrossRef] [PubMed]

30. Cao, X.H.; Tan, C.L.; Sindoro, M.; Zhang, H. Hybrid micro/nano-structures derived from metal-organic frameworks: Preparation and applications in energy storage and conversion. *Chem. Soc. Rev.* **2017**, *46*, 2660–2677. [CrossRef]

31. Xia, W.; Mahmood, A.; Zou, R.Q.; Xu, Q. Metal-organic frameworks and their derived nanostructures for electrochemical energy storage and conversion. *Energy Environ. Sci.* **2015**, *8*, 1837–1866. [CrossRef]

32. Dhakshinamoorthy, A.; Li, Z.H.; Garcia, H. Catalysis and photocatalysis by metal organic frameworks. *Chem. Soc. Rev.* **2018**, *47*, 8134–8172. [CrossRef] [PubMed]

33. Stassen, I.; Burtch, N.; Talin, A.; Falcaro, P.; Allendorf, M.; Ameloot, R. An updated roadmap for the integration of metal-organic frameworks with electronic devices and chemical sensors. *Chem. Soc. Rev.* **2017**, *46*, 3185–3241. [CrossRef] [PubMed]

34. Wu, M.X.; Yang, Y.W. Metal-Organic Framework (MOF)-Based Drug/Cargo Delivery and Cancer Therapy. *Adv. Mater.* **2017**, *29*, 1606134–1606153. [CrossRef] [PubMed]

35. Li, J.; Wang, X.X.; Zhao, G.X.; Chen, C.L.; Chai, Z.F.; Alsaedi, A.; Hayat, T.; Wang, X.K. Metal-organic framework-based materials: Superior adsorbents for the capture of toxic and radioactive metal ions. *Chem. Soc. Rev.* **2018**, *47*, 2322–2356. [CrossRef] [PubMed]

36. Li, X.; Liu, Y.X.; Wang, J.; Gascon, J.; Li, J.S.; Bruggen, B.V. Metal-organic frameworks based membranes for liquid separation. *Chem. Soc. Rev.* **2017**, *46*, 7124–7144. [CrossRef]

37. Xia, Q.; Wang, H.; Huang, B.B.; Yuan, X.Z.; Zhang, J.J.; Zhang, J.; Jiang, L.B.; Xiong, T.; Zeng, G.M. State-of-the-art advances and challenges of iron-based metal organic frameworks from attractive features, synthesis to multifunctional applications. *Small* **2018**, *15*, 1803088. [CrossRef] [PubMed]

38. Xu, X.D.; Cao, R.G.; Jeong, S.; Cho, J. Spindle-like mesoporous α-Fe$_2$O$_3$ anode material prepared from MOF template for high-rate lithium batteries. *Nano Lett.* **2012**, *12*, 4988–4991. [CrossRef]

39. Zhou, T.T.; Zhang, R.; Wang, Y.B.; Zhang, T. MOF-derived 1D α-Fe$_2$O$_3$/NiFe$_2$O$_4$ heterojunction as efficient sensing materials of acetone vapors. *Sens. Actuators B Chem.* **2019**, *281*, 885–892. [CrossRef]

40. Zhng, Y.L.; Jia, C.W.; Wang, Q.Y.; Kong, Q.; Chen, G.; Guan, H.T.; Dong, C.J. Highly Sensitive and Selective Toluene Sensor of Bimetallic Ni/Fe-MOFs Derived Porous NiFe2O4 Nanorods. *Ind. Eng. Chem. Res.* **2019**, *58*, 9450–9457. [CrossRef]

41. Dong, C.J.; Liu, X.; Xiao, X.C.; Chen, G.; Wang, Y.D.; Djerdj, I. Combustion synthesis of porous Pt-functionalized SnO$_2$ sheets for isopropanol gas detection with a significant enhancement in response. *J. Mater. Chem. A* **2014**, *2*, 20089–20095. [CrossRef]

42. Dong, C.J.; Jiang, M.; Tao, Y.; Shen, Y.Y.; Lu, Y.X.; Yuan, Y.; Wang, Y.D. Nonaqueous synthesis of Pd-functionalized SnO$_2$/In$_2$O$_3$ nanocomposites for excellent butane sensing properties. *Sens. Actuators B Chem.* **2018**, *257*, 419–426. [CrossRef]

43. Ferrari, M.; Lutterotti, L. Method for the simultaneous determination of anisotropic residual stresses and texture by X-ray diffraction. *J. Appl. Phys.* **1994**, *76*, 7246. [CrossRef]

44. Zhu, D.Z.; Jiang, J.X.; Sun, D.M.; Qian, X.Y.; Wang, Y.W.; Li, L.C.; Wang, Z.W.; Chai, X.L.; Gan, L.H.; Liu, M.X. A general strategy to synthesize high-level N-doped porous carbons via Schiff-base chemistry for supercapacitors. *J. Mater. Chem. A* **2018**, *6*, 12334–12343. [CrossRef]

45. Zhang, R.; Zhou, T.T.; Wang, L.L.; Zhang, T. Metal-organic frameworks (MOFs) derived hierarchical Co$_3$O$_4$ structures as efficient sensing materials for acetone detection. *ACS Appl. Mater. Interfaces* **2018**, *10*, 9765–9773. [CrossRef]

46. Jeong, H.-M.; Kim, J.-H.; Jeong, S.-Y.; Kwak, C.-H.; Lee, J.-H. Co$_3$O$_4$−SnO$_2$ Hollow Heteronanostructures: Facile Control of Gas Selectivity by Compositional Tuning of Sensing Materials via Galvanic Replacement. *ACS Appl. Mater. Interfaces* **2016**, *8*, 7877–7883. [CrossRef]

47. Zhou, X.; Li, X.W.; Sun, H.B.; Sun, P.; Liang, X.S.; Liu, F.M.; Hu, X.L.; Lu, G.Y. Nanosheet-Assembled ZnFe$_2$O$_4$ Hollow Microspheres for High-Sensitive Acetone Sensor. *ACS Appl. Mater. Interfaces* **2015**, *7*, 15414–15421. [CrossRef]

48. Yuan, C.X.; Li, H.R.; Xie, L.Z.; Wang, F.; Deng, H.; Chang, F.Z.; Sun, Y.Z. Flower-like NiO nanostructures synthesized by electrodeposition method for efficient detection of toluene gas. *RSC Adv.* **2015**, *5*, 92128–92133. [CrossRef]

49. Liu, H.Y.; He, Y.H.; Nagashima, K.; Meng, G.; Dai, T.T.; Tong, B.; Deng, Z.H.; Wang, S.M.; Zhu, N.W.; Yanagida, T.; et al. Discrimination of VOCs molecules via extracting concealed features from a emperature-modulated p-type NiO sensor. *Sens. Actuators B Chem.* **2019**, *293*, 342–349. [CrossRef]

50. Yang, C.; Xiao, F.; Wang, J.D.; Su, X.T. 3D flower- and 2D sheet-like CuO nanostructures: Microwave-assisted synthesis and application in gas sensors. *Sens. Actuators B Chem.* **2015**, *207*, 177–185. [CrossRef]

51. Wang, L.L.; Deng, J.N.; Lou, Z.; Zhang, T. Nanoparticles-assembled Co$_3$O$_4$ nanorods p-type nanomaterials: One-pot synthesis and toluene-sensing properties. *Sens. Actuators B Chem.* **2014**, *201*, 1–6. [CrossRef]

52. Zhao, C.H.; Huang, B.Y.; Zhou, J.Y.; Xie, E.Q. Synthesis of porous Co$_3$O$_4$ nanonetworks to detect toluene at low concentration. *Phys. Chem. Chem. Phys.* **2014**, *16*, 19327–19332. [CrossRef]

53. Cao, J.; Wang, S.; Zhang, H.; Zhang, T. Facile construction of Co_3O_4 porous microspheres with enhanced acetone gas sensing performances. *Mater. Sci. Semicond. Proc.* **2019**, *101*, 10–15. [CrossRef]

54. Ma, H.; Xu, Y.; Rong, Z.; Cheng, X.; Gao, S.; Zhang, X.; Zhao, H.; Huo, L. Highly toluene sensing performance based on monodispersed Cr_2O_3 porous microspheres. *Sens. Actuators B Chem.* **2012**, *174*, 325–331. [CrossRef]

55. Chen, M.P.; Zhang, D.M.; Hu, J.C.; Wang, H.P.; Zhang, Y.M.; Li, K.J.; Rong, Q.; Zhou, S.Q.; Zhang, J.; Zhu, Z.Q.; et al. Excellent toluene gas sensing properties of molecular imprinted Ag-$LaFeO_3$ nanostructures synthesized by microwave-assisted process. *Mater. Res. Bull.* **2019**, *111*, 320–328. [CrossRef]

56. Chen, H.; Ao, S.S.R.; Li, G.D.; Gao, Q.; Zou, X.X.; Wei, C.D. Enhanced sensing performance to toluene and xylene by construvting NiGa2O4-NiO heterostructures. *Sens. Actuators B Chem.* **2019**, *282*, 331–338. [CrossRef]

57. Lai, X.; Gao, K.; Shen, G.; Xue, P.; Wang, D.; Hu, F.; Zhang, J.; Yang, Q.; Wang, X. Ordered mesoporous $NiFe_2O_4$ with ultrathin framework for low-ppb toluene sensing. *Sci. Bull.* **2018**, *63*, 187–193. [CrossRef]

58. Kim, B.Y.; Yoon, J.W.; Kim, J.K.; Kang, Y.C.; Lee, J.H. Dual role of multiroom-structured Sn-doped NiO microspheres for ultrasensitive and highly selective detection of xylene. *ACS Appl. Mater. Interfaces* **2018**, *10*, 16605–16612. [CrossRef]

59. Huang, Y.; Wang, Y.R.; Hu, Q.; Mu, X.M.; Zhang, Y.X.; Bai, J.L.; Wang, Q.; Shen, Y.Z.; Shen, Z.X.; Xie, E.Q. A low temperature and highly sensitive ethanol sensor based on Au modified In_2O_3 nanofibers by coaxial electrosponning. *J. Mater. Chem. C* **2018**, *6*, 10935–10943. [CrossRef]

60. Franke, M.E.; Koplin, T.J.; Simon, U. Metal and metal oxide nanoparticles inchemiresistors: Does the nanoscale matter? *Small* **2006**, *2*, 36–50. [CrossRef]

61. Tudorache, F.; Popa, P.D.; Dobromir, M.; Iacomi, F. Studies on the structure and gas sensing properties of nickel–cobalt ferrite thin films prepared by spin coating. *Mater. Sci. Eng. B* **2013**, *178*, 1334–1338. [CrossRef]

62. Dumitrescu, A.M.; Lisa, G.; Iordan, A.R.; Tudorache, F.; Petrila, I.; Borhan, A.I.; Palamaru, M.N.; Mihailescu, C.; Leontie, L.; Munteanu, C. Ni ferrite highly organized as humidity sensors. *Mater. Chem. Phys.* **2015**, *156*, 170–179. [CrossRef]

63. Gurlo, T.A.; Bârsan, N.; Weimar, U. Basics of oxygen and SnO_2 interaction: Work function change and conductivity measurements. *Sens. Actuators B Chem.* **2006**, *118*, 78–83. [CrossRef]

64. Zou, Y.Z.; Wang, H.; Yang, R.S.; Lai, X.Y.; Wan, J.W.; Lin, G.; Liu, D. Controlled synthesis and enhanced toluene-sensing properties of mesoporous $Ni_xCo_{1-x}Fe_2O_4$ nanostructured microspheres with tunable composite. *Sens. Actuators B Chem.* **2019**, *280*, 227–234. [CrossRef]